Journal of Materials Chemistry A

ROYAL SOCIETY OF CHEMISTRY

PAPER

View Article Online
View Journal | View Issue

Check for updates

Cite this: J. Mater. Chem. A, 2025, 13, 2650

A highly efficient metal-free electrocatalyst of nitrogen-doped porous carbon nanoflowers toward oxygen electroreduction†

Xiaoli Fan,[a] Yingying Zhang,*[a] Longlong Fan,[a] Qinghong Geng,[a] Wei Zhu,[a] Esmail Doustkhah[c] and Cuiling Li *[b]

Received 8th October 2024
Accepted 9th December 2024

DOI: 10.1039/d4ta07178f

rsc.li/materials-a

Metal-free catalysts offer a desirable alternative to traditional metal-based catalysts. However, it remains challenging to improve the catalytic performance of metal-free catalysts to be as promising as that of metal-based materials. Herein, a polymer-assisted method followed by pyrolysis treatment was employed to synthesize nitrogen (N)-doped porous carbon nanoflowers with nanosheet subunits. Leveraging the unique geometry structure and abundant pyridinic-N active sites, the optimized catalyst exhibits a good half-wave potential of 0.85 V *versus* reversible hydrogen electrode (*vs.* RHE) and long-term stability with only 17.0 mV negative shift of the half-wave potential after 10 000 cyclic voltammetry cycles in alkaline electrolyte. This research presents a viable strategy for advancing metal-free catalysts.

1 Introduction

Metal–air batteries are widely advocated as a promising candidate for next-generation energy storage systems due to their high energy density and low cost.[1–3] The overall efficiency of metal–air batteries deeply depends on the oxygen reduction reaction (ORR).[4,5] However, the inherent sluggish kinetics of ORR processes pose significant challenges to the development of high-performance ORR electrocatalysts.[6,7] Although metal-based catalysts, such as Pt and Fe, have demonstrated satisfactory ORR performance, their industrial applications remain limited by various drawbacks, including prohibitive cost (especially for precious metals) and serious agglomeration of metal nanoparticles during electrochemical processes.[8] Therefore, the exploration of an economical and resourceful metal-free electrocatalyst with high performance is highly desirable for the sustainable development and large-scale application of metal–air batteries.

Recently, nitrogen (N)-doped porous carbon materials with different dimensional nanostructures, such as one-dimensional nanotubes, two-dimensional nanosheets and three-dimensional structures, have been widely applied in many energy-related fields.[9–12] Among them, carbon nanosheets, especially those derived from zeolitic imidazolate frameworks-8 (ZIF-8) nanosheets, have been widely employed as catalysts in various electrochemical fields, owing to their high surface area and adequate active site accessibility.[13–15] Self-agglomeration of carbon nanosheets usually occurs in electrocatalytic applications, thus resulting in insufficient utilization of the advantages of nanosheets. Assembly of two-dimensional nanosheets into three-dimensional micro/nanostructures provides an alternative way to efficiently prevent the self-agglomeration drawbacks of two-dimensional nanosheets, which is critical for demonstrating the merits of two-dimensional materials.[16,17] Therefore, N-doped porous carbon nanoflowers assembled by carbon nanosheets may be a promising electrocatalyst with superior ORR activity.

Herein, a polymer-assisted approach was employed to fabricate ZIF-8-based nanoflowers, in which polydopamine (PDA) drives the evolution of ZIF-8 nanosheets into assembled nanoflowers and polyvinyl pyrrolidone (PVP) induces the dispersion of nanoflowers. N-doped porous carbon nanoflowers (N-PCNFs) with nanosheet subunits were obtained by pyrolysis of the obtained ZIF-8-based nanoflowers. Due to the superb and abundant pyridinic-N active sites, the obtained N-PCNFs exhibit enhanced catalytic performance toward electrochemical ORR. Among all the samples, the N-doped porous carbon nanoflowers with a pyridinic-N content of 43.5% (N-PCNFs-43.5) exhibit optimized ORR activity with a half-wave potential of 0.85 V, comparable to that of the commercial Pt/C-20% catalyst.

2 Results and discussion

2.1. Synthesis and characterization of ZIF-8-based nanoflowers

The synthetic procedure for the metal-free catalysts was briefly illustrated in Fig. 1a and the detailed experiments can be found

[a]School of Chemistry and Chemical Engineering, Beijing Institute of Technology, Beijing 100081, China. E-mail: zhangyingying@bit.edu.cn

[b]CAS Key Laboratory of Bio-Inspired Materials and Interface Science, Technical Institute of Physics and Chemistry, Chinese Academy of Sciences, Beijing 100190, China. E-mail: licuiling@mail.ipc.ac.cn

[c]Chemistry Department, Faculty of Engineering and Natural Sciences, Istinye University, Sariyer, Istanbul 34396, Turkey

† Electronic supplementary information (ESI) available. See DOI: https://doi.org/10.1039/d4ta07178f

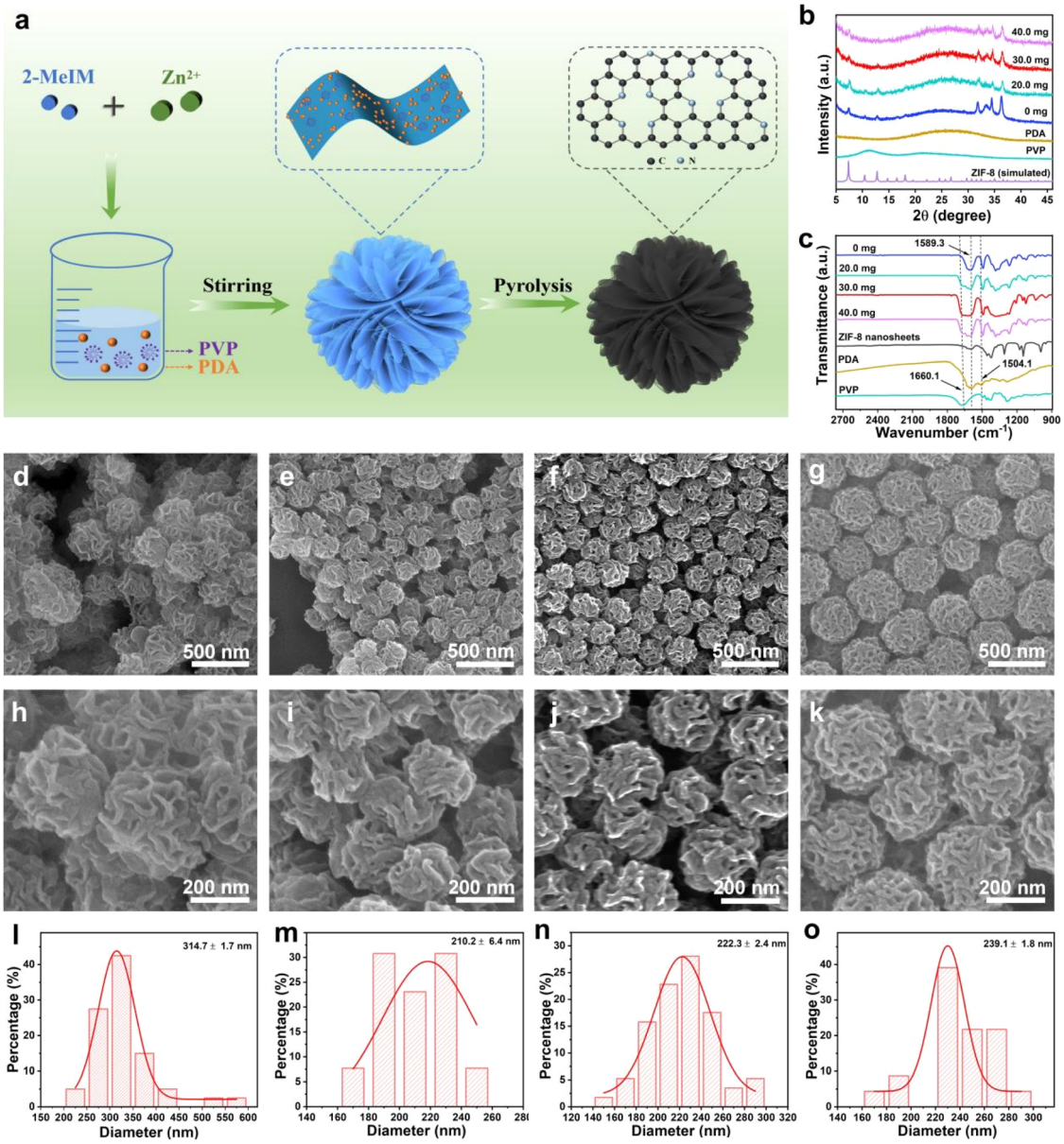

Fig. 1 (a) The schematic illustration for the preparation procedure of N-PCNFs. (b) XRD patterns of PVP, PDA and ZIF-8-based nanoflowers prepared with different dosage of PVP. (c) FTIR spectra of ZIF-8 nanosheets, PVP, PDA and ZIF-8-based nanoflowers prepared with different dosages of PVP. (d–g) Low- and (h–k) high-magnification SEM images and (l–o) corresponded size distribution of products synthesized with different dosage of PVP: (d, h and l) 0 mg, (e, i and m) 20.0 mg, (f, j and n) 30.0 mg and (g, k and o) 40.0 mg.

in the ESI.† In the synthetic procedure, a certain amount of PVP (*e.g.*, 0, 20.0, 30.0 or 40.0 mg) and dopamine (80.0 mg) were firstly dissolved in a mixed solution of deionized water and methanol (volume ratio of 1 : 1). Subsequently, liquid ammonia was added to induce the polymerization of dopamine. Then, 2-methylimidazole (2-MeIM) and $Zn(NO_3)_2$ were sequentially added to this mixture. After mixing the reagents, zinc ions will coordinate with 2-MeIM to form ZIF-8. The obtained products were collected and characterized by powder X-ray diffraction (XRD). The observed diffraction peaks at 7.4°, 10.5°, 12.9°, 31.6°, 32.5°, 34.6° and 36.7° corresponded to the (110), (200), (211), (600), (611), (541) and (444) diffraction planes of ZIF-8, respectively, verifying the formation of ZIF-8 under the synthetic condition (Fig. 1b).[18–22] Meanwhile, the obvious broad diffraction peak located at 25.0° was attributed to PDA.[23] The resultant product was then characterized by Fourier transform infrared (FTIR). Specifically, the peaks at approximately 1504.1 and 1589.3 cm^{-1} corresponded to the stretching vibrations of the indole structure of polydopamine molecule, indicating the formation of PDA in the obtained sample.[23,24] As previous studies demonstrated that the polymerization of dopamine underwent phenolic hydroxyl oxidation, Michael addition, and aromatization rearrangement reactions to form PDA in the existence of oxygen (Fig. S1†).[23] As a result, dopaminequinone

and 5,6-dihydroxyindole were newly formed in the PDA, which were absent in the dopamine precursor. Considering the structure differences between dopamine and PDA molecules, the typical peaks corresponding to the indole structure in the FTIR spectra can be used as evidence for the successful formation of PDA. Meanwhile, the peak centred at approximately 1660.1 cm^{-1} was ascribed to the stretching vibration of carbonyl, indicating the presence of PVP.[25] Additionally, multiple absorption peaks in the wavenumber ranging from 900.1 to 1480.1 cm^{-1} were assigned to the stretching or bending vibrations of the imidazole ring, supporting the presence of 2-MeIM in all the samples (Fig. 1c).[20,21] The existence of PVP and PDA in the obtained sample may be attributed to the weak coordination interactions between zinc ions and the carbonyl in PVP or the amine in PDA.[18,23] All the FTIR and XRD measurements consistently demonstrated that ZIF-8 capping with PVP and PDA was successfully synthesized, and the sample was denoted as PVP-PDA-modified ZIF-8. Scanning electron microscope (SEM) was then employed to characterize the morphology of the obtained products synthesized under different conditions. As revealed, nanoflowers with uniformly distributed particle size were obtained. More importantly, the morphology of obtained products gradually changed from loosely assembled nanoflowers to compact nanoflowers as the feeding amount of PVP was increased from 0 to 20.0, 30.0 and 40.0 mg (Fig. 1d–k). Such kind of morphology regulation can be attributed to the strong shaping effect of PVP molecules.[26] Besides the structural regulation effect of PVP molecules, PDA also played a crucial role in the formation of nanoflowers. The morphology can be continuously tuned from nanosheets to loosely assembled nanoflowers, and ultimately to nanoflowers when the dopamine feeding amount was increased from 0 mg to medium (20.0 and 60.0 mg), and high values (80.0 and 100.0 mg) (Fig. S2†). Of note, the nanosheet structured product was confirmed to be ZIF-8 by XRD analysis (Fig. S3†). Hence, this variability in the morphology of the precursors suggested that PDA could induce the evolution of ZIF-8 nanosheets into nanoflowers. Compared with other samples, the diffraction peaks of ZIF-8 in the product obtained with 100.0 mg of dopamine was significantly reduced (Fig. S3†). Consequently, a dopamine feeding amount of

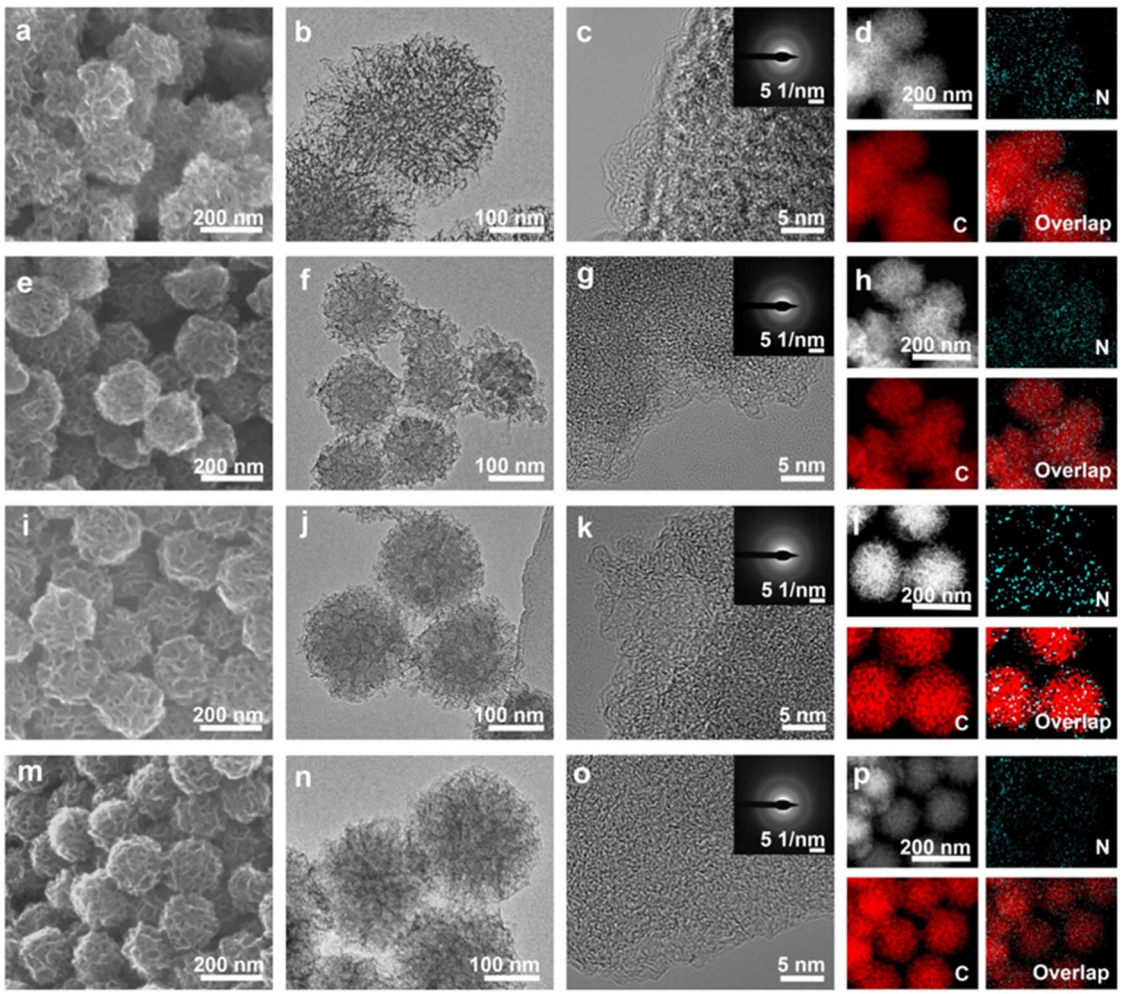

Fig. 2 (a, e, i and m) SEM, (b, f, j and n) TEM, (c, f, k and o) HR-TEM (inset: SAED pattern) and (d, h, l and p) HAADF-STEM images and corresponding element mapping images of different N-PCNFs samples: (a–d) PCNFs-9.6, (e–h) N-PCNFs-13.3, (i–l) N-PCNFs-43.5 and (m–p) N-PCNFs-17.0.

80.0 mg was chosen for subsequent experiments. In the absence of 2-MeIM and $Zn(NO_3)_2$ precursors, nanosheet structured PDA can be obtained (Fig. 1c and S4†). Based on the above results, the formation of highly dispersed ZIF-8-based nanoflowers was attributed to the building units of ZIF-8 nanosheets under the nanosheet-directing effect of PDA and capping effect of PVP molecules. Furthermore, the morphology evolution of nanoflower structures was explored by isolating the products at different reaction intervals and characterized by SEM. As shown from the SEM images, nanosheets were initially formed at the initial stage (30.0 min), which were then etched and aggregated to form assembled nanoparticles (35.0 min and 45.0 min). With the reaction proceeded, the assembled nanoparticles gradually grew to form well-defined nanoflowers (Fig. S5†). Consequently, an optimal reaction time of 120.0 min was chosen for obtaining nanoflower structured products.

2.2. Characterization of N-doped porous carbon nanoflowers

The resultant ZIF-8-based nanoflowers assembled from nanosheets, which were synthesized with different feeding amount of PVP (*e.g.*, 0, 20.0, 30.0 or 40.0 mg), were then carbonized at 1000 °C in an argon atmosphere. The XRD patterns of all the pyrolyzed samples exhibited a broad peak at 22.0°, which is the characteristic of disordered carbon structure (Fig. S6†).[6] Subsequently, the morphology of the obtained samples was characterized by SEM and transition electron microscopy (TEM). Both SEM (Fig. 2a, e, i and m) and TEM images (Fig. 2b, f, j, n) revealed that all the final samples retained the assembled nanoflower structures. In comparison to the ZIF-8-based nanoflowers precursor, a slight decrease of particle size can be observed for the pyrolyzed products (Fig. 1l–o and S7†), which can be attributed to the structure shrinkage of ZIF-8-based nanoflowers precursor during pyrolysis process. The high resolution TEM (HR-TEM) image and selected area electron diffraction (SAED) pattern revealed the amorphous structure of all the pyrolyzed samples (Fig. 2c, g, k and o), which are consistent with the XRD results. The high-angle annular dark-field scanning TEM (HAADF-STEM) and the elemental mapping images confirmed the uniform distribution of C and N elements in all the pyrolyzed samples (Fig. 2d, h, l and p). To investigate the porous features of all the pyrolyzed samples, nitrogen adsorption–desorption measurements were conducted. The N_2 adsorption–desorption isotherms of all the pyrolyzed samples displayed a steep increase in the micropore region at a relatively low N_2 partial pressure and a well-defined hysteresis loop at higher pressure, confirming the existence of micropores and mesopores in all the pyrolyzed samples (Fig. 3a). The pore size distribution revealed that most of the mesopores were concentrated at 2–5 nm (Fig. 3b). Previous research suggested that micropores were essential for hosting more active sites and small mesopores (between 2 and 4 nm) can efficiently facilitate the access of reactants to internal active sites and increase the accessibility of active sites.[27,28] Therefore, the hierarchical meso/microporous structure of all the pyrolyzed samples contributed to a high external surface area (Table S1†), which is beneficial for enhancing the ORR property.

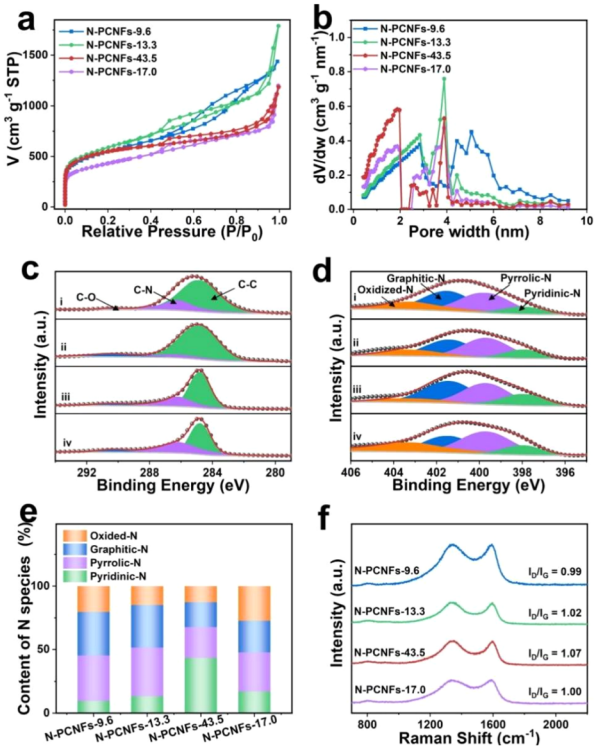

Fig. 3 (a) N_2 adsorption–desorption isotherms and (b) pore-size distributions of different N-PCNFs samples. High-resolution XPS spectra of (c) C 1s and (d) N 1s for (i) N-PCNFs-9.6, (ii) N-PCNFs-13.3, (iii) N-PCNFs-43.5 and (iv) N-PCNFs-17.0, respectively. (e) The relative contents of oxidized-N, graphitic-N, pyrrolic-N and pyridinic-N species and (f) Raman spectra of N-PCNFs samples PCNFs samples.

X-ray photoelectron spectroscopy (XPS) was employed to elucidate the surface composition and elemental valence states of all the final samples (Fig. S8†). The corresponding high-resolution C 1s spectra were fitted into three carbon species including C–C (284.8 eV), C–N (286.2 eV) and C═O (290.4 eV) (Fig. 3c). The presence of C–N species indicated successful doping of N atoms into the carbon skeleton.[29,30] All the above results verified that N-doped porous carbon nanoflowers (N-PCNFs) were formed. The high-resolution N 1s spectra of N-PCNFs were deconvoluted into four peaks comprising pyridinic-N at 397.9 eV, pyrrolic-N at 399.7 eV, graphitic-N at 401.4 eV and oxidized-N at 403.2 eV, respectively (Fig. 3d).[31–33] Then, the content of different N species was quantitatively analyzed and summarized (Fig. 3e and Table S2†). The resultant N-PCNFs derived from ZIF-8-based nanoflowers synthesized by using different PVP feeding amounts (0, 20.0, 30.0 or 40.0 mg) exhibited variations in the N species. The pyridinic-N species has been demonstrated to be active for electrocatalyzing ORR through the four-electron pathway.[31,32] Therefore, the pyridinic-N content was utilized to distinguish the obtained N-PCNFs samples, and the final sample name was abbreviated as N-PCNFs-*x*, where *x* represents the percentage of pyridinic-N in all N species. The ZIF-8-based nanoflowers obtained by using 0, 20.0, 30.0 and 40.0 mg of PVP delivered N-PCNFs-9.6, N-PCNFs-13.3, N-PCNFs-43.5 and N-PCNFs-17.0, respectively. Doping of heteroatom always lead to an increase in defects in the carbon

substrate. These defects usually played an essential role in the catalytic performance of ORR. The degree of defects of N-PCNFs was characterized by Raman spectroscopy measurement (Fig. 3f). The peaks at 1350.1 and 1580.3 cm^{-1} corresponded to the disordered carbon (D band) and graphitic carbon (G band), respectively. The intensity ratio of D band to G band (I_D/I_G) indicates the defect density of carbon materials.[31–34] The calculated I_D/I_G value of N-PCNFs-43.5 was 1.07, outstripping those of N-PCNFs-9.6 (0.99), N-PCNFs-13.3 (1.02) and N-PCNFs-17.0 (1.01), suggesting more defect sites in N-PCNFs-43.5. More defects usually changed the electronic distribution of the neighboring carbon atoms and activated the adsorbed oxygen molecules, thereby enhancing the ORR catalytic activity.

2.3. Electrocatalytic oxygen reduction performance

Inspired by their electrical conductivity and unique geometric structure, the obtained N-PCNFs samples were expected to evoke promising electrochemical ORR performances. To evaluate their ORR performance, all the N-PCNFs samples were evaluated in N_2- or O_2-saturated 0.1 M KOH electrolyte by using rotating disk electrode (RDE). The commercial Pt/C-20% catalyst was selected as benchmark and evaluated under same conditions. As shown in the typical cyclic voltammetry (CV) curves recorded in N_2- or O_2-saturated 0.1 M KOH, obvious reduction peaks appear in the CV curves obtained in O_2-saturated electrolyte for all the samples (Fig. 4a), indicating that all the N-PCNFs samples have ORR activity.[6] To gain deeper insight into the ORR performance, linear sweep voltammetry (LSV) measurement was performed. The ORR onset potential of N-PCNFs-43.5 was 0.97 V, which is close to the commercial Pt/C-20% (1.00 V). Among all the N-PCNFs samples, N-PCNFs-43.5 exhibited a half-wave potential (0.85 V), which exceeds that of commercial Pt/C-20% catalyst (0.84 V), N-PCNFs-9.6 (0.81 V), N-PCNFs-13.3 (0.83 V), and N-PCNFs-17.0 (0.75 V) (Fig. 4b and c). Moreover, N-PCNFs-43.5 showed a higher half-wave potential in comparison to catalysts derived from different pyrolytic temperatures (Fig. S9a†). The elevated high half-wave potential can be attributed to the abundant content of graphitic-N (Fig. S9b†), which facilitates electron transfer. Importantly, the half-wave potential and onset potential of N-PCNFs-43.5

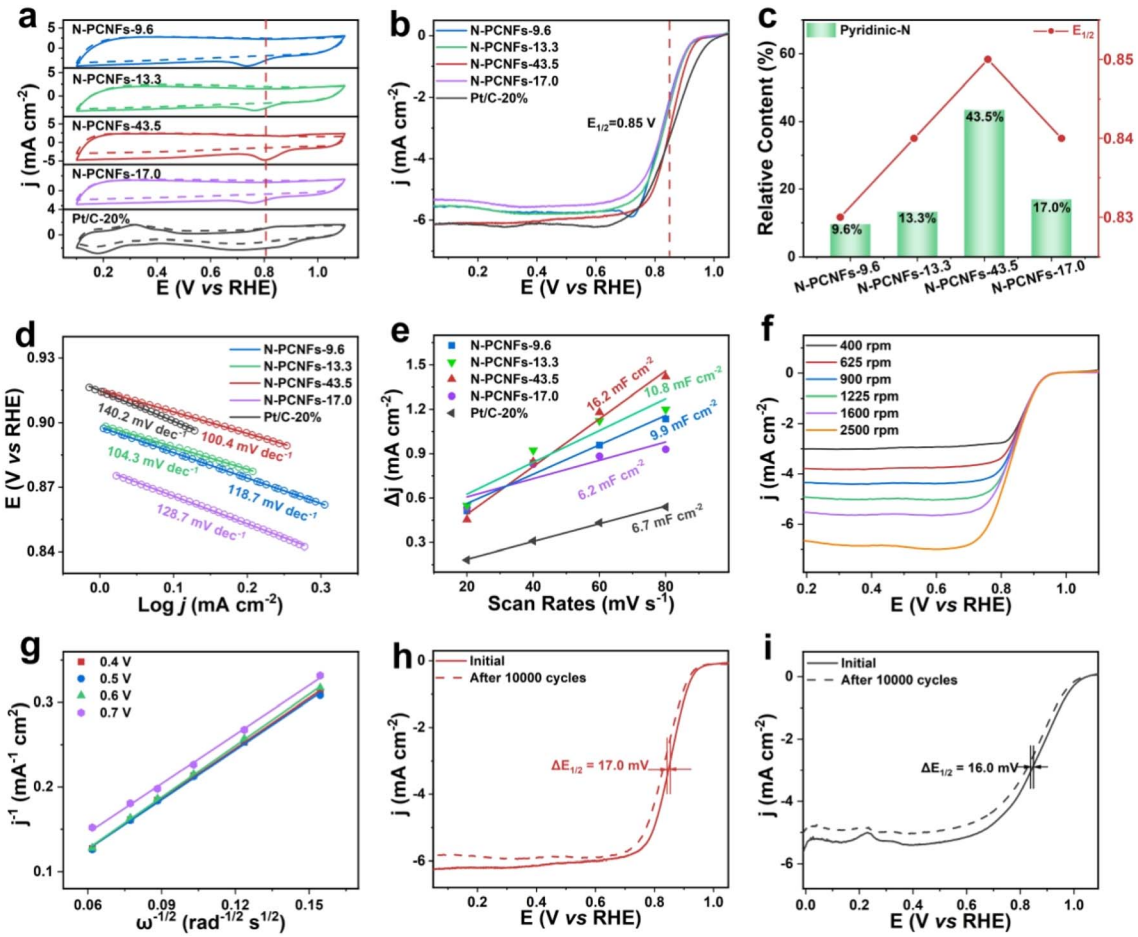

Fig. 4 (a) CV curves of the electrocatalysts with a scan rate of 50 mV s^{-1} in N_2- and O_2-saturated 0.1 M KOH electrolyte. (b) ORR polarization curves of N-PCNFs and commercial Pt/C-20% catalyst in O_2-saturated 0.1 M KOH electrolyte at a rotation rate of 1600 rpm. (c) Comparison of half-wave potential and the content of pyridinic-N in different samples. (d) Tafel plots and (e) electrochemical double layer capacitance (C_{dl}) values of N-PCNFs and commercial Pt/C-20% catalyst. (f) LSV curves at various rotation speeds and (g) the corresponding K–L plots of N-PCNFs-43.5. LSV curves of (h) N-PCNFs-43.5 and (i) commercial Pt/C-20% catalyst in O_2-saturated 0.1 M KOH electrolyte at 1600 rpm before and after 10 000 cyclic voltammetry cycles.

were better than that of recently reported ORR electrocatalysts (Table S3†).[35–44]

To investigate the catalytic kinetics, Tafel slopes of all the samples were obtained based on LSV curves. The corresponding Tafel slope of N-PCNFs-43.5 (100.4 mV dec^{-1}) was lower than that of N-PCNFs-9.6 (118.7 mV dec^{-1}), N-PCNFs-13.3 (104.3 mV dec^{-1}) and N-PCNFs-17.0 (128.7 mV dec^{-1}), indicating the fast ORR kinetics of N-PCNFs-43.5 (Fig. 4d). The fast reaction kinetics of N-PCNFs-43.5 may be related to its intrinsic electrocatalytic activity. To better understand the intrinsic electrocatalytic activity of N-PCNFs-43.5, the electrochemical surface areas (ECSA) were investigated by measuring the double-layer capacitance (C_{dl}), which were estimated by using the CV curves with different sweep rates between 1.0 and 1.1 V *vs.* RHE (Fig. S10† and 4e).[43] The calculated C_{dl} and ECSA values of N-PCNFs-43.5 were estimated to be 16.2 mF cm^{-2} and 405.0 m^2 g^{-1}, respectively, which are larger than those of N-PCNFs-9.6 (9.9 mF cm^{-2}, 247.5 m^2 g^{-1}), N-PCNFs-13.3 (10.8 mF cm^{-2}, 270.0 m^2 g^{-1}) and N-PCNFs-17.0 (6.2 mF cm^{-2}, 155.0 m^2 g^{-1}) (Table S1†). This may be because N-PCNFs-43.5 possesses the highest external surface area, which is beneficial for increasing the number of accessible active sites and improving their utilization.[28] The electrochemical ORR performance of nitrogen-doped porous carbon nanosheets (N-PCNSs) derived from pyrolyzing ZIF-8 nanosheets were also investigated under the same condition (Fig. S11†). Despite of the same composition of N-PCNFs and N-PCNSs, their ORR performance deviates greatly (Fig. S12†), further demonstrating the critical role of the N-doped porous carbon samples in electrocatalyzing ORR.

Afterward, the RDE tests were conducted at different rotation speeds to better understand the ORR pathway of the N-PCNFs samples and commercial Pt/C-20% catalyst (Fig. 4f and S13†). According to the Koutecky–Levich (K–L) equation, the electron transfer number (n) was calculated for all the samples, and the n values for N-PCNFs-9.6, N-PCNFs-13.3, N-PCNFs-43.5, N-PCNFs-17.0 and commercial Pt/C-20% catalyst were 3.9, 3.9, 4.0, 3.8 and 4.0, respectively (Fig. 4g and S14†). All the results indicate that the oxygen reduction catalyzed by N-PCNFs-43.5 takes the four-electron transfer pathway. Furthermore, the catalytic durability of N-PCNFs-43.5 and commercial Pt/C-20% catalyst was investigated at the potential between 0.6 and 0.9 V in O_2-saturated electrolytes. After 10 000 cyclic voltammetry cycles, the half-wave potential exhibited a negative shift of 17.0 mV for N-PCNFs-43.5 (Fig. 4h), which was comparable to commercial Pt/C-20% catalyst (16.0 mV) (Fig. 4i). The excellent durability of N-PCNFs-43.5 in electrocatalyzing ORR was probably attributed to the superior morphology stability (Fig. S15†).

3 Conclusions

In summary, we have demonstrated N-doped porous carbon nanoflowers as efficient metal-free electrocatalysts for ORR. The N-PCNFs with optimal pyridine-N content and porous structure (N-PCNFs-43.5) exhibit a half-wave potential of 0.85 V in alkaline electrolyte, which is comparable with the commercial Pt/C-20% catalyst (0.84 V). Even after 10 000 cyclic voltammetry cycles, the half-wave potential of N-PCNFs-43.5 showed a negative shift of 17.0 mV, which is comparable to the commercial Pt/C-20% catalyst (16.0 mV). The superior performance with robust durability was mainly attributed to the unique porous carbon nanoflower structures, which not only benefit the exposure and accessibility of active sites but also enable efficient charge-transfer properties. This study introduces novel insights into the design of highly active metal-free ORR electrocatalysts with great promise for practical applications.

Data availability

All relevant date are presented in the main text and ESI.†

Author contributions

X. L. Fan performed the experiments and analyzed the data. Y. Y. Zhang helped the electrochemical measurement and wrote the manuscript. L. L. Fan performed SEM characterization studies. Q. H. Geng did the TEM characterization. W. Zhu performed some synthetic experiments. E. Doustkhah helped revise the manuscript. C. L. Li designed the experiments and revised the manuscript as well as supervised the project.

Conflicts of interest

There are no conflicts to declare.

Acknowledgements

The authors acknowledge the Analysis and Testing Centre in Beijing Institute of Technology for technical support.

Notes and references

1 Y. X. Zhang, W. H. Xiao, T. T. Hu, S. X. Hu, H. Q. Wang, M. J. Zhou, Z. H. Hou, Y. Liu and B. H. He, Metal-organic frameworks-inspired design of highly efficient nitrogen-doped carbon nanoflower electrocatalysts for Zn-air batteries, *J. Mater. Sci.*, 2023, **58**, 8157–8168.
2 X. X. Wang, X. Yang, H. Liu, T. Han, J. Hu, H. Li and G. Wu, Air electrodes for flexible and rechargeable Zn-air batteries, *Small Struct.*, 2021, **3**, 2100103–2100111.
3 Z. Song, J. Ding, B. Liu, X. Liu, X. Han, Y. Deng, W. Hu and C. Zhong, A rechargeable Zn-air battery with high energy efficiency and long life enabled by a highly waterretentive gel electrolyte with reaction modifier, *Adv. Mater.*, 2020, **32**, 1908127–1908137.
4 R. Mercado, F. Nichols and S. W. Chen, Nitrogen-doped carbon flowers with Fe and Ni dual metal centers for effective electroreduction of oxygen, *Inorganics*, 2022, **10**, 36–45.
5 X. Wang, R. K. M. Raghupathy, C. J. Querebillo, Z. Liao, D. Li, K. Lin, M. Hantusch, Z. Sofer, B. Li, E. Zschech, I. M. Weidinger, T. D. Kuhne, H. Mirhosseini, M. Yu and X. Feng, Interfacial covalent bonds regulated electron-

deficient 2D black phosphorus for electrocatalytic oxygen reactions, *Adv. Mater.*, 2021, **33**, 2008752–2008780.

6 J. X. Li, L. L. Fan, Q. F. Hua, Q. H. Geng, Y. Y. Zhang, X. L. Fan, L. Ma, C. M. Wang, W. Zhu, X. Feng and C. L. Li, Ordered macroporous carbonous skeletons implanted with dual-phase Co/CoFe nanoparticles for boosting electrocatalytic performance, *Chem. Eng. J.*, 2023, **470**, 144399–144406.

7 K. Gong, F. Du, Z. Xia, M. Durstock and L. Dai, Nitrogen-doped carbon nanotube arrays with high electrocatalytic activity for oxygen reduction, *Science*, 2009, **323**, 760–764.

8 T. J. Zhao, L. Y. Zhu, J. Tang, L. Fu, D. Jiang, X. Q. Wei, H. Nara, T. Asahi and Y. Yamauchi, Enhancing electrocatalytic performance *via* thickness-tuned hollow N-doped mesoporous carbon with embedded Co nanoparticles for oxygen reduction reaction, *ACS Nano*, 2024, **18**, 373–382.

9 Y. Zheng, Y. Jiao and S. Z. Qiao, Engineering of carbon-based electrocatalysts for emerging energy conversion: From fundamentality to functionality, *Adv. Mater.*, 2015, **27**, 5372–5378.

10 W. Ni and L. Y. Shi, Review article: Layer-structured carbonaceous materials for advanced Li-ion and Na-ion batteries: Beyond graphene, *J. Vac. Sci. Technol., A*, 2019, **37**, 040803–040839.

11 S. Farid, S. Z. Ren, D. X. Tian, W. W. Qiu, J. L. Zhao, L. L. Zhao, Q. Mao and C. Hao, 3D flower-like polypyrrole-derived N-doped porous carbon coupled cobalt oxide as efficient oxygen evolution electrocatalyst, *Int. J. Hydrogen Energy*, 2020, **45**, 31926–31941.

12 H. X. Gang, S. C. Chen, J. B.-H. Tok and Z. N. Bao, An emerging class of carbon materials: Synthesis and applications of carbon flowers, *Matter*, 2023, **6**, 2206–2234.

13 J. Xu, X. Y. Chen, Y. S. Xu, Y. P. Du and C. H. Yan, Ultrathin 2D rare-earth nanomaterials: Compositions, syntheses, and applications, *Adv. Mater.*, 2020, **32**, 1806461–1806478.

14 W. H. He, C. H. Jiang, J. Wang and L. H. Lu, High-rate oxygen electroreduction over graphitic-N species exposed on 3D hierarchically porous nitrogen-doped carbons, *Angew. Chem., Int. Ed.*, 2014, **126**, 9657–9661.

15 Y. Jiang, H. Q. Liu, X. H. Tan, L. M. Guo, J. T. Zhang, S. N. Liu, Y. J. Guo, J. Zhang, H. F. Wang and W. G. Chu, Monoclinic ZIF-8 nanosheet-derived 2D carbon nanosheets as sulfur immobilizer for high-performance lithium sulfur batteries, *ACS Appl. Mater. Interfaces*, 2017, **9**, 25239–25249.

16 W. Q. Qian, S. W. Xu, X. M. Zhang, C. B. Li, W. Y. Yang, C. R. Browen and Y. Yang, Differences and similarities of photocatalysis and electrocatalysis in two-dimensional nanomaterials: Strategies, traps, applications and challenges, *Nano-Micro Lett.*, 2021, **13**, 156–194.

17 M. C. Wu, X. Hu, W. Y. Zheng, L. Y. Chen and Q. C. Zhang, Recent advances in porous carbon nanosheets for high-performance metal-ion capacitors, *Chem. Eng. J.*, 2023, **466**, 143077–1431102.

18 L. Gang, S. Z. Li, Z. Guo, Q. K. Farha, B. G. Hauser, X. Y. Qi, Y. Wang, X. Wang, S. Y. Han, X. G. Liu, J. S. Duchene, H. Zhang, Q. C. Zhang, X. D. Chen, J. Ma, S. C. J. Loo, W. D. Wei, Y. H. Yang, J. T. Hupp and F. W. Huo, Imparting functionality to a metal-organic framework material by controlled nanoparticle encapsulation, *Nat. Chem.*, 2012, **4**, 310–316.

19 Y. X. Xing, L. Wang, L. C. Wang, L. X. Huang, S. Wang, X. Y. Xie, J. Zhu, T. Ding, K. Y. Cai and J. X. Zhang, Flower-like nanozymes with large accessibility of single atom catalysis sites for ROS generation boosted tumor therapy, *Adv. Funct. Mater.*, 2021, **32**, 2111171–2111186.

20 A. M. Aboraia, A. A. A. Darwish, V. Polyakov, E. Erofeeva, V. Butova, H. Y. Zahran, A. F. Abd El-Rehim, H. Algarni, I. S. Yahia and V. Soldatov, Structural characterization and optical properties of zeolitic imidazolate frameworks (ZIF-8) for solid-state electronics applications, *Opt. Mater.*, 2020, **100**, 109648–109655.

21 P. J. Shao, Y. Shen, J. X. Be, J. K. Zhao, L. D. Wang and S. H. Zhang, Shape controlled ZIF-8 crystals for carbonic anhydrase immobilization to boost CO_2 uptake into aqueous MDEA solution, *Sep. Purif. Technol.*, 2023, **315**, 123683–123693.

22 S. P. Wu, W. J. Shi, L. J. Cui and C. Xu, Enhancing contaminant rejection efficiency with ZIF-8 molecular sieving in sustainable mixed matrix membranes, *Chem. Eng. J.*, 2024, **482**, 148954–14148967.

23 Y. H. Deng, W. Liu, R. Xu, N. Huang, Y. Zheng, Y. P. Huang, H. Li, X. Y. Kong and L. Q. Ye, Reduction of superoxide radical intermediate by polydopamine for efficient hydrogen peroxide photosynthesis, *Angew. Chem., Int. Ed.*, 2024, **63**, 202319216–202319225.

24 J. Park, I. Hyun, Y. K. Kim, H. Jung, D. M. Lee, S. W. Kim and S. U. Son, A very small amount (0.1 wt%) of $Co(OH)_2$ nanoplates enhances triboelectric performance of polymers, *J. Mater. Chem. A*, 2024, **12**, 12397–12404.

25 F. Yang, S. J. Wang, Z. Z. Li, Y. C. Xu, W. T. Yang, C. X. Yv, D. C. Yang, Y. Xie and W. Zhou, Polydopamine/defective ultrathin mesoporous graphitic carbon nitride nanosheets as Z-scheme organic assembly for robust photothermal-photocatalytic performance, *J. Colloid Interface Sci.*, 2022, **613**, 775–785.

26 K. M. Koczkur, S. Mourdikoudis, L. Polavarapu and S. E. Skrabalak, Polyvinylpyrrolidone (PVP) in nanoparticle synthesis, *Dalton Trans.*, 2015, **44**, 17883–17905.

27 W. K. Zhu, H. T. Liu, Y. B. Pei, T. Liu, J. F. Zhang, X. Liu, L. Q. Wang, Y. J. Feng, Y. Yin and M. D. Guiver, Defect-engineered ZIF-derived non-Pt cathode catalyst at 1.5 mg cm^{-2} loading for proton exchange membrane fuel cells, *Small*, 2023, **19**, 2302090–2302100.

28 J. H. Zheng, G. N. Guo, H. W. Li, L. Wang, H. J. Yu, Y. C. Yan and A. G. Dong, Elaborately designed micro-mesoporous graphitic carbon spheres as efficient polysulfide reservoir for lithium-sulfur batteries, *ACS Energy Lett.*, 2017, **5**, 1105–1114.

29 B. L. Jiang, N. Jiang, Y. Y. Cui, H. Wang, G. Zhang, Y. H. Zhang, Q. Zhang, L. Li, Z. S. Jin, C. G. Wang, L. Y. Zhang and Z. M. Su, Rapid synthesis and microenvironment optimization of hierarchical porous Fe-

N-C catalysts for enhanced ORR in microbial fuel cells, *Adv. Sci.*, 2024, **11**, 2402610–2402623.

30 M. S. Liu, T. Sun, T. Y. Peng, J. Q. Wu, J. H. Li, S. L. Chen, L. Zhang, S. Li, J. M. Zhang and S. H. Sun, Fe-NC single-atom catalyst with hierarchical porous structure and P-O bond coordination for oxygen reduction, *ACS Energy Lett.*, 2023, **8**, 4531–4539.

31 Y. Y. Liu, F. D. Tu, Z. Y. Zhang, Z. G. Zhao, P. Guo, L. X. Shen, Y. L. Zhang, L. Zhao, G. J. Shao and Z. B. Wang, Molecular scissor tailoring hierarchical architecture of ZIF-derived Fe/N/C catalysts for acidic oxygen reduction reaction, *Appl. Catal., B*, 2023, **324**, 122209–122219.

32 W. Peng, J. X. Liu, X. Q. Liu, L. Q. Wang, L. C. Yin, H. T. Tan, F. Hou and J. Liang, Facilitating two-electron oxygen reduction with pyrrolic nitrogen sites for electrochemical hydrogen peroxide production, *Nat. Commun.*, 2023, **14**, 4430–4441.

33 R. Zhao, Z. B. Liang, S. Gao, C. Yang, B. J. Zhu, J. L. Zhao, C. Qu, R. Q. Zhao and Q. Xu, Puffing up energetic metal-organic frameworks to large carbon networks with hierarchical porosity and atomically dispersed metal sites, *Angew. Chem., Int. Ed.*, 2019, **58**, 1975–1979.

34 Y. Q. Zhang, X. L. Zhang, X. X. Ma, W. H. Guo, C. C. Wang, T. Asefa and X. Q. He, A facile synthesis of nitrogen-doped highly porous carbon nanoplatelets: efficient catalysts for oxygen electroreduction, *Sci. Rep.*, 2017, **7**, 43366–43376.

35 J. H. Roh, A. Cho, S. J. Kim, K. S. Lee, J. Shin, J. S. Choi, J. Bak, S. J. Lee, D. H. Song, E. J. Kim, C. Lee, Y. R. Uhm, Y. H. Cho, J. W. Han and E. A. Cho, Transformation of the active moiety in phosphorus-doped Fe-N-C for highly efficient oxygen reduction reaction, *ACS Catal.*, 2023, **13**, 9427–9441.

36 L. T. Cui, L. R. Cui, Z. J. Li, J. Zhang, H. N. Wang, S. F. Lu and Y. Xiang, A copper single-atom catalyst towards efficient and durable oxygen reduction for fuel cells, *J. Mater. Chem. A*, 2019, **7**, 16690–16695.

37 M. M. Fan, Q. X. Yuan, Y. Y. Zhao, Z. M. Wang, A. Wang, Y. Y. Liu, K. Sun, J. J. Wu, L. Wangh and J. C. Jiang, A facile "double-catalysts" approach to directionally fabricate pyridinic N-B-pair-doped crystal graphene nanoribbons/amorphous carbon hybrid electrocatalysts for efficient oxygen reduction reaction, *Adv. Mater.*, 2022, **34**, 2107040–2107051.

38 G. Saianand, A. I. Gopalan, J. C. Lee, C. Sathish, K. Gopalakrishnan, G. E. Unni, D. Shanbhag, V. D. B. C. Dasireddy, J. Yi, S. Xi, A. A. H. Almuhtaseb and A. Vinu, Mixed copper/copper-oxide anchored mesoporous fullerene nanohybrids as superior electrocatalysts toward oxygen reduction reaction, *Small*, 2020, **16**, 1903937–1903948.

39 M. M. Tong, F. F. Sun, Y. Xie, Y. Wang, Y. Q. Yang, C. G. Tian, L. Wang and H. G. Fu, Operando cooperated catalytic mechanism of atomically dispersed Cu-N_4 and Zn-N_4 for promoting oxygen reduction reaction, *Angew Chem. Int. Ed. Engl.*, 2021, **60**, 14005–14012.

40 J. Wang, Z. Huang, W. Liu, C. Chang, H. Tang, Z. Li, W. Chen, C. Jia, T. Yao, S. Wei, Y. Wu and Y. D. Li, Design of N-coordinated dual-metal sites: A stable and active Pt-free catalyst for acidic oxygen reduction reaction, *J. Am. Chem. Soc.*, 2017, **139**, 17281–17284.

41 Y. Meng, J. Yin, T. Jiao, J. Bai, L. Zhang, J. Su, S. Liu, Z. Bai, M. Cao and Q. Peng, Self-assembled copper/cobalt-containing polypyrrole hydrogels for highly efficient ORR electrocatalysts, *J. Mol. Liq.*, 2020, **298**, 112010–112018.

42 A. Arunchander, S. G. Peera, S. K. Panda, S. Chellammal and A. K. Sahu, Simultaneous co-doping of N and S by a facile in-situ polymerization of 6-N,N-dibutylamine-1,3,5-triazine-2,4-dithiol on graphene framework: An efficient and durable oxygen reduction catalyst in alkaline medium, *Carbon*, 2017, **118**, 531–544.

43 Z. Zhang, J. Sun, F. Wang and L. Dai, Efficient oxygen reduction reaction (ORR) catalysts based on single iron atoms dispersed on a hierarchically structured porous carbon framework, *Angew Chem. Int. Ed. Engl.*, 2018, **57**, 9038–9043.

44 X. X. Wang, D. A. Cullen, Y. T. Pan, S. Hwang, M. Wang, Z. Feng, J. Wang, M. H. Engelhard, H. Zhang, Y. He, Y. Shao, D. Su, K. L. More, J. S. Spendelow and G. Wu, Nitrogen-coordinated single cobalt atom catalysts for oxygen reduction in proton exchange membrane fuel cells, *Adv. Mater.*, 2018, **30**, 1706758–1706767.